

# 14 Advanced Measurement Methods in Time Domain Reflectometry for Soil Moisture Determination

Christof Huebner<sup>1</sup>, Stefan Schlaeger<sup>2</sup>, Rolf Becker<sup>3</sup>, Alexander Scheuermann<sup>4</sup>, Alexander Brandelik<sup>5</sup>, Wolfram Schaedel<sup>3</sup>, Rainer Schuhmann<sup>5</sup>

<sup>1</sup>Fachhochschule Mannheim – University of Applied Sciences

<sup>2</sup>Research Center Karlsruhe, Institute of Technical Chemistry, Water and Geotechnology Section

<sup>3</sup>University of Karlsruhe, Institute of Water Resources Management, Hydraulic and Rural Engineering

<sup>4</sup>University of Karlsruhe, Institute of Rock Mechanics and Soil Mechanics

<sup>5</sup>Research Center Karlsruhe, Institute of Meteorology and Climate Research

## 14.1 Introduction

Knowledge of soil moisture is essential to many applications in hydrology, agriculture, and civil engineering. Among the various electromagnetic or dielectric moisture measurement methods time domain reflectometry (TDR) has become one of the most used methods. This is due to the early establishment of simple approximate relations between soil dielectric properties and water content and the availability of field portable instruments [1]. Sensors used for TDR usually consist of two- or three-wire transmission lines which are buried into the soil and connected to a TDR set-up (Fig. 14.1). A fast rise time (about 200 ps) voltage step is launched into a coaxial cable and propagates through the sensor system. At the transition between the coaxial cable and the two-wire transmission line a part of the pulse is reflected due to impedance mismatch. The remaining pulse travels along the two-wire line until it is totally reflected at the open end. An oscilloscope records the sum of the incident signal and the reflected signal (step response), also called the TDR trace, from which the travel time and the mean wave velocity in the two-wire line section can be determined. The permittivity of the surrounding soil can be calculated from the wave velocity and is related to the mean soil water content. For many applications this basic TDR measurement method is not sufficient for user requirements. The most serious limitations are

1. the restricted length of the transmission line (usually not more than 30 cm),
2. the lack of spatial water content resolution along the transmission line, and
3. the lack of a low-cost high-precision TDR instrument.

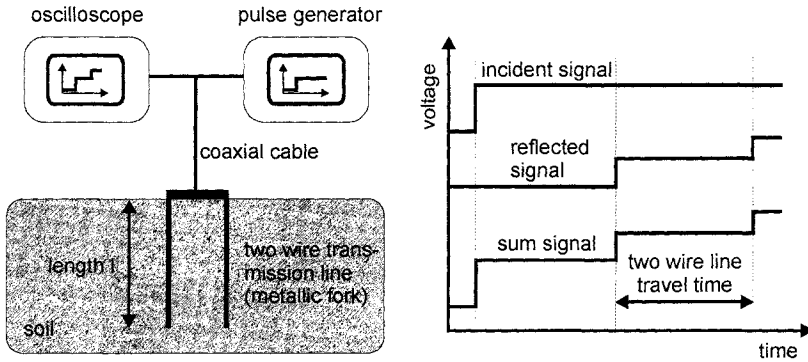


**Fig. 14.1.** Basic TDR set-up and signals. Oscilloscope and pulse generator are usually integrated in a single TDR instrument

Therefore a new transmission line technology, a reconstruction algorithm for determining the water content profile along the transmission line and a new TDR instrument have been developed and will be presented in this work. Experimental results, e.g., obtained in a project dealing with water transport processes in a full-scale levee model, demonstrate the applicability of the proposed methods for practical problems.

## 14.2 Dielectric Properties of Soils

TDR as an electromagnetic moisture measurement method is an indirect way to determine water content. The relation between water content and electrically measured permittivity of the soil has to be established by calibration. Though this is not the focus of this work, some of the most important definitions and dielectric properties of soils are reviewed.

Definitions of water content are different in various scientific or industrial fields, e.g., a weight-related definition (dry or wet) is preferred in soil mechanics and civil engineering whereas hydrologists ask for volume-related water content to evaluate the transport equations. As the dielectric measurement is a volumetric phenomenon, we agree on a volumetric definition of the water content  $W$ . Conversion into gravimetric water content or saturation requires additional information on dry density or pore fraction.

The straightforward but most laborious way to find the relation between the water content and permittivity of a soil is to perform a site-specific calibration with gravimetric sampling. This is often impracticable for operational use and does not allow sensor performance prediction prior to installation. Therefore, several empirical, semi-empirical, and theoretical mixing rules with different degrees of experimental justification have been developed and applied. One of the

most often used empirical equations was given by Topp et al [2] for the soil permittivity  $\epsilon_m$ :

$$\epsilon_m = 3.03 + 9.3 W + 146 W^2 - 76.7 W^3. \quad (14.1)$$

This approach with a real-valued permittivity is valid as long as losses in the measurement frequency range can be neglected, which is not true for soils with high clay and/or salt content. To apply a reconstruction algorithm for water content profile determination it is crucial to know the frequency-dependent complex permittivity of the soil. One approach is a simple model based on the refractive mixing rule developed by Birchak et al [3]:

$$\sqrt{\epsilon_m} = W \sqrt{\epsilon_w} + S \sqrt{\epsilon_s} + A \sqrt{\epsilon_a}. \quad (14.2)$$

$S$ ,  $W$ , and  $A$  are the volumetric fractions of solid particles, water, and air with their corresponding permittivities  $\epsilon_s$ ,  $\epsilon_w$ , and  $\epsilon_a$ . The permittivity of water is considered to be complex valued due to its ionic conductivity  $\sigma_w$  and therefore depends on the frequency  $f$ .  $\epsilon_{ws}$  is the static permittivity of water. Thus

$$\epsilon_w = \epsilon_{w,real} - j \epsilon_{w,imag} = \epsilon_{ws} - j \frac{\sigma_w}{2\pi f \epsilon_0}. \quad (14.3)$$

This simple model is compared to measurements on sand and clay materials in Fig. 14.2 and Fig. 14.3. The sand exhibits very low losses and a nearly frequency-independent real part of the permittivity except at very low frequencies. It can be expected that this trend will remain up to about 1 GHz until water relaxation smoothly starts to decrease the real part of the permittivity and increase dielectric losses.

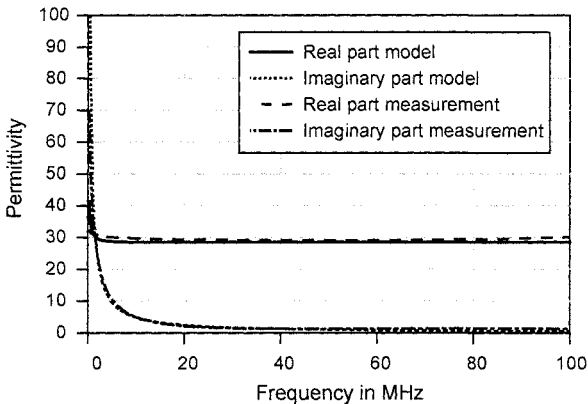


**Fig. 14.2.** Frequency-dependent complex permittivity of a sand material ( $S = 0.5$ ,  $W = 0.455$ ,  $A = 1 - W - S$ ,  $\epsilon_w = 80$ ,  $\epsilon_s = 6$ ,  $\epsilon_a = 1$ ,  $\sigma_w = 0.01$  S/m)

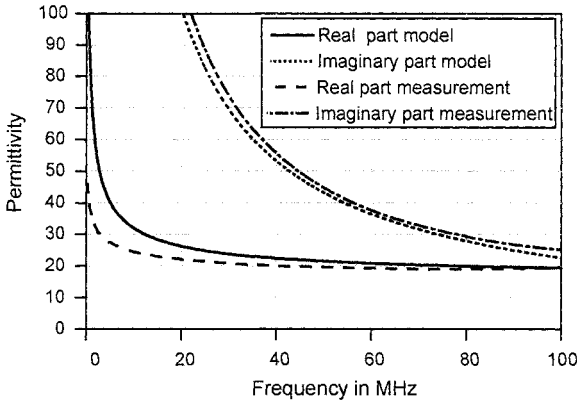


**Fig. 14.3.** Frequency-dependent complex permittivity of a clay material ( $S = 0.6$ ,  $W = 0.35$ ,  $A = 1 - W \cdot S$ ,  $\epsilon_w = 80$ ,  $\epsilon_s = 3$ ,  $\epsilon_a = 1$ ,  $\sigma_w = 0.8$  S/m)

The frequency dependence of the clay is much more pronounced due to the high conductivity. Furthermore the quality factor  $\epsilon_{real}/\epsilon_{imag}$  is less than 1 even at frequencies as high as 100 MHz.

Though this simple model is in close agreement with the measurement results, it does not take into account the relaxation of water, temperature-dependent permittivities, nor bound water which is especially found in clayey soil. Nevertheless the general trend is clearly visible. More sophisticated models of the dielectric properties of soils have been investigated by Dobson et al [4] and Heimovaara et al [5] and compared to experimental results.

Soil moisture measurements should be preferably carried out at frequencies where losses are small. TDR, however, is an inherently broadband method with a frequency range from a few kilohertz up to several gigahertz. Fortunately the standard travel time analysis of TDR traces can approximately be considered as a measurement in the frequency range between about 100 MHz and 1 GHz. The relatively small dependency of the TDR method on soil type is attributed to this high-frequency measurement [6].

The use of a reconstruction algorithm to determine the water content profile along the transmission line implies the analysis of the amplitude variations of the TDR trace. Therefore losses cannot be neglected and the frequency-dependent permittivity has to be accounted for. Losses also limit the maximum length of the transmission line, because the electromagnetic pulses are attenuated and disappear on longer lines. The upper limit is about 1 m depending on the conductivity [7]. In order to overcome this limitation a new transmission line technology has been developed and will be discussed in the next section.

### 14.3 Transmission Lines

For longer transmission lines we propose insulated flexible flat band cables. They show much less pulse attenuation than non-insulated metallic forks in the same media. Several cables with different geometries have been developed and manufactured, from simple concentric insulation to sophisticated multiwire structures with unilateral sensitivity [8, 9]. The flat band cable used for most experiments here is shown in Fig. 14.4 together with its electrical field distribution in cross-section. The cable consists of three copper wires covered with polyethylene insulation. The electrical field is concentrated around the conductors and defines the sensitive area of 3 to 5 cm around the cable. The spatial weighting of the measurement in the cross-section of the cable is directly related to the energy density distribution. In order to predict the time domain response of the cable the electromagnetic properties have to be measured or calculated by numerical methods. The well-known equivalent circuit for an infinitesimal section of a transmission line is shown in Fig. 14.5. The equivalent circuit parameters are the series resistance  $R$ , inductance  $L$ , shunt conductance  $G$  and capacitance  $C$ .

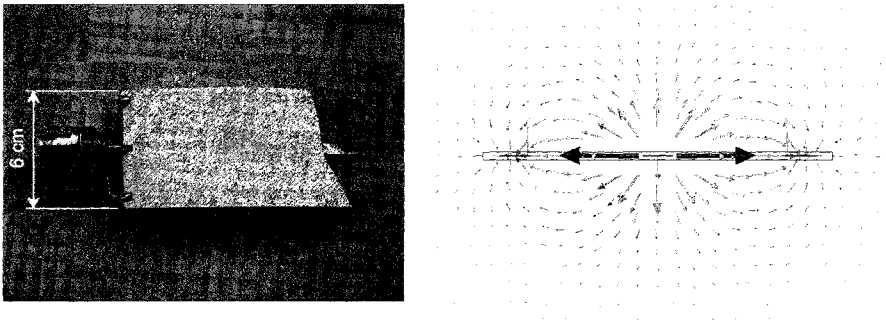


**Fig. 14.4.** Flat band cable and electrical field distribution in cross-section for symmetric excitation (inner conductor positive, outer conductors negative)

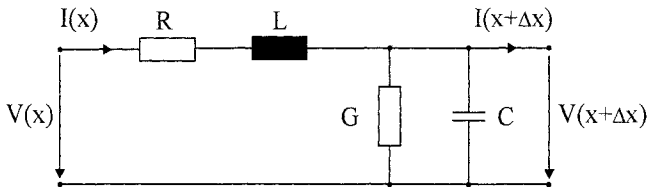


**Fig. 14.5.** Equivalent circuit of an infinitesimal section of a transverse electromagnetic (TEM) transmission line.  $V(x)$  and  $I(x)$  are the voltage and the current at the beginning and at the end of the line

A limitation of this model is that radiation and higher order modes are not included. Open-wire lines exhibit electromagnetic radiation when the electrical spacing between the wires is large. Then they behave as a hybrid transmission line/antenna mixture. Radiation strongly increases with frequency and may be a major source of loss and rise time degradation. Future investigations will focus on this important aspect but require full-wave numerical field simulations. Nevertheless the equivalent circuit in Fig. 14.5 is a reasonable approach for calculating the wave propagation along the transmission line.

### 14.3.1 Resistance R and Inductance L

The resistive losses are due to the skin effect. At low frequencies there is a uniform distribution of the current through the cross-section of the copper conductors. As the frequency increases, current concentrates at the edges of the conductors, and at the highest frequency most of the current is flowing in a very thin region. This behavior is illustrated in Fig. 14.6 and Fig. 14.7 which show the cross-section of the cable with its magnetic field distribution at 1 MHz and the current density in the outer left conductor at four different frequencies.

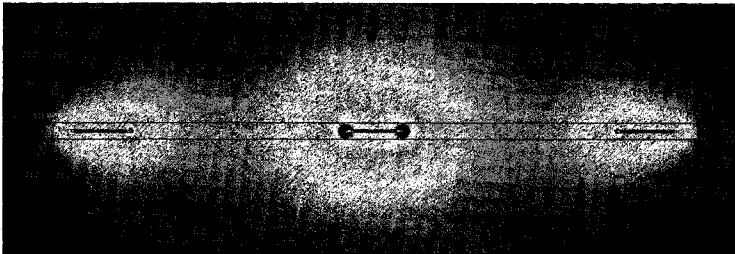


Fig. 14.6. Magnetic field distribution in the cross-section of the cable at 1 MHz



Fig. 14.7. Current density in the outer left conductor for four different frequencies. As frequency increases the current concentrates at the edges of the conductor. The dark color in the middle of the conductor represents low current density

As the frequency increases, the cross-sectional area available for current flow decreases and causes an increase in series resistance (Fig. 14.8). In most practical cases resistance losses are small compared with dielectric losses (shunt conductance) except for long cables in nearly lossless materials like snow. For the same reason that resistance is frequency dependent, the inductance will be too. As the current distribution changes, the internal self-inductance decreases with frequency (Fig. 14.8). At the highest frequency only the external inductance will remain. The transition frequency is around 100 kHz. This means that within the usual time window of TDR measurements (< 100 ns) no significant influence of the inductance increase at low frequencies will be expected.

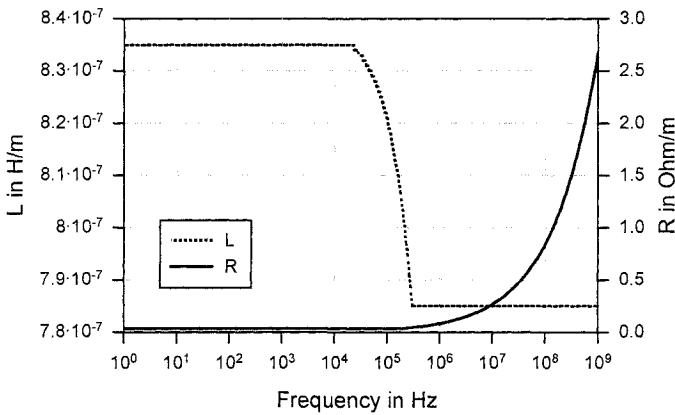
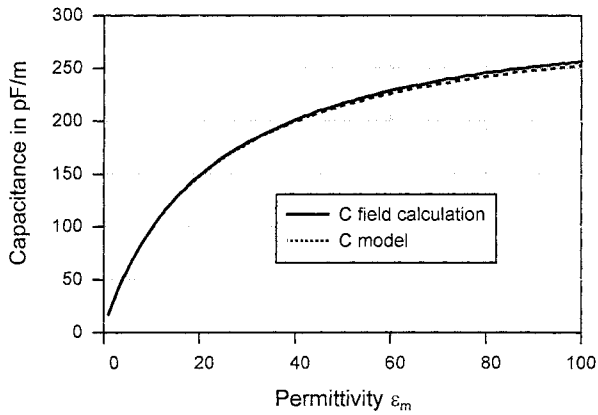


Fig. 14.8. Series resistance and inductance of the flat band cable for symmetric excitation (stepwise interpolated data based on numerical field simulation)

### 14.3.2 Capacitance C and Conductance G

Unlike resistance and inductance, capacitance and conductance are dependent on the dielectric properties of the soil surrounding the cable. Both C and G can be determined with numerical field calculation. For the lossless case (G = 0) the relation between real permittivity  $\epsilon_m$  and capacitance C shown in Fig. 14.9 has been obtained. A simple model with three capacitances is able to explain this behavior. The capacitance C may be replaced by  $C_1$ ,  $C_2$  and  $\epsilon_m C_3$  as shown in Fig. 14.10. The total capacitance is given by

$$C(\epsilon_m) = C_1 + \frac{C_2 \epsilon_m C_3}{C_2 + \epsilon_m C_3} \tag{14.4}$$



**Fig. 14.9.** Relation between permittivity and capacitance for the lossless case and symmetric excitation of the cable (cf. Fig. 14.4)

The three unknown capacitances  $C_1$ ,  $C_2$ , and  $C_3$  were derived from numerical field calculation and calibration measurements with three different media around the cable (Table 14.1).

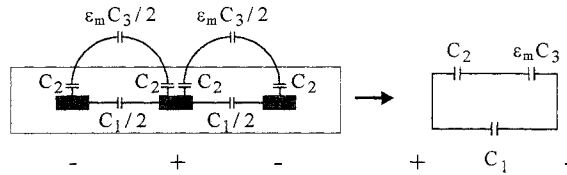


**Fig. 14.10.** Capacitance model of the flat band cable

**Table 14.1.** Parameters of the three-capacitance model

Circuit element	$C_1$	$C_2$	$C_3$
Measured	3.4 pF/m	323 pF/m	14.8 pF/m
Calculated	4.0 pF/m	303 pF/m	13.7 pF/m

The differences between measurement and calculation are attributed to the uncertainty in measuring the thickness of the insulation, which is a very sensitive parameter, especially at high permittivities. With some limitations at high conductivities, Eq. (14.4) is a good approximation for complex permittivities as well. The DC conductivity of the soil,  $\sigma_m$ , can be combined with real permittivity and frequency with a complex permittivity:

$$\epsilon_m = \epsilon_{m,real} - j\epsilon_{m,imag} = \epsilon_{m,real} - j \frac{\sigma_m}{2\pi f \epsilon_0}. \tag{14.5}$$



Then  $C$  and  $G$  are calculated according to the following equation:

$$C(\varepsilon_m) + j \frac{G(\varepsilon_m)}{2\pi f} = C_1 + \frac{C_2 \varepsilon_m C_3}{C_2 + \varepsilon_m C_3} \quad (14.6)$$

$C_1$  and  $C_2$  contribute to  $G$  as well due to dielectric losses in the polyethylene ( $\tan \delta \approx 2 \times 10^{-4}$ ), but these are usually very small compared to losses caused by soil conductivity and can therefore be neglected. Even when the soil has a frequency-independent real permittivity and conductivity the equivalent circuit parameters  $C$  and  $G$  of an insulated transmission line are dispersive, which is a kind of Maxwell-Wagner effect [10]. Figure 14.11 shows the frequency dependence of  $C$  and  $G$  for real permittivity  $\varepsilon = 1$  and conductivity  $\sigma = 0.1, 0.01, \text{ and } 0.001 \text{ S/m}$ .

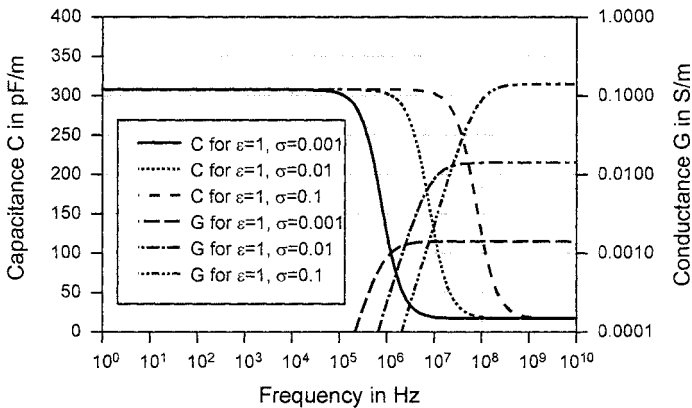


**Fig. 14.11.** Capacitance  $C$  and conductance  $G$  of the flat band cable embedded in a material with real permittivity  $\varepsilon = 1$  and conductivity  $\sigma = 0.1, 0.01, \text{ and } 0.001 \text{ S/m}$

At low frequencies the capacitance is strongly enhanced and conductivity is near zero. Lower conductivity corresponds to lower transition frequencies and consequently has less influence on the TDR trace in the usually short time range. In order to study these effects the transient response of a transmission line under various conditions will be calculated in the next section.

### 14.3.3 Transient Analysis

The transient response of a transmission line can be calculated in the time domain or by Laplace/Fourier transformation from the frequency to the time domain. The advantage of a frequency to time domain transformation is the easy incorporation of dispersive equivalent circuit parameters. Time domain methods on the other hand are usually limited to non-dispersive  $L$ ,  $C$ ,  $R$ , and  $G$ . Their advantage is the availability of fast and robust inversion algorithms for the reconstruction of

inhomogeneous  $C$  and  $G$  profiles along transmission lines, which are required for many soil moisture measurement applications. Fortunately inversion algorithms usually analyze only once or twice the time range to the reflection at the open end of the transmission line. Within this time range the assumption of non-dispersive equivalent circuit parameters may be a good approximation. Figure 14.12 shows the transient response of a 1 m long flat band cable embedded in two materials with different conductivities. Within the time range up to the reflection at the open end at about 18 ns the agreement for the low-loss case is good. The deviation for the high-loss case is greater. For longer times the TDR traces diverge more and more. At infinity the TDR trace in the dispersive case reaches a level of 2 V due to zero conductivity of the insulated flat band cable at DC.

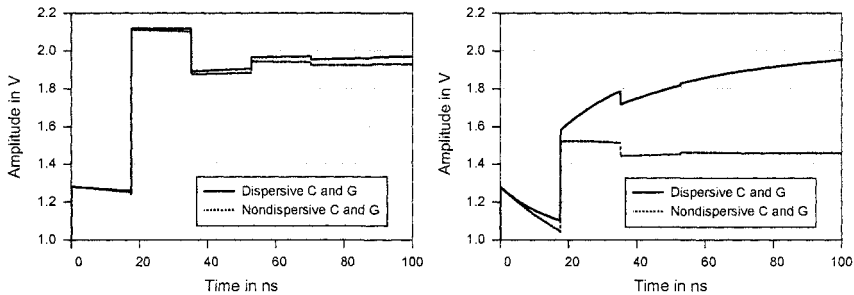


**Fig. 14.12.** Simulation of the TDR trace of a 1 m long flat band cable; 1 V step as incident signal. *Left:* dispersive  $C$  and  $G$  ( $\epsilon_{m,real} = 10$ ,  $\sigma_m = 0.001$  S/m, Eqs. (14.5-6)), non-dispersive  $C$  and  $G$  ( $C = 98.6$  pF/m,  $G = 0.00074$  S/m) *Right:* dispersive  $C$  and  $G$  ( $\epsilon_{m,real} = 10$ ,  $\sigma_m = 0.01$  S/m, Eqs. (14.5-6)), non-dispersive  $C$  and  $G$  ( $C = 98.6$  pF/m,  $G = 0.0074$  S/m)

## 14.4 Reconstruction Algorithm

The standard TDR measurement procedure based on travel time analysis delivers only the mean water content along the transmission line. On the other hand many applications require soil moisture profiles to be determined. One approach to satisfy these demands has been developed by Hook et al [11]. The transmission line is divided into several sections by remote-controlled switches. This solution only allows a very coarse spatial resolution of the soil moisture distribution. A high spatial resolution can be achieved by exploiting the full information in the reflected electromagnetic signal. Each change in water content along the transmission line means an impedance change and a partial reflection. A three-step algorithm has been developed to reconstruct the soil moisture profile from these reflections [12].

In the first step the transmission line parameters  $C(x)$  and  $G(x)$  are reconstructed with two independent time domain measurements from both ends of the flat cable by solving the inverse problem for the telegraph equations. If there

are only one-sided reflections available it is possible to reconstruct  $C(x)$  with a given distribution of  $G(x)$ . The second step transforms  $C(x)$  into the dielectric coefficient  $\varepsilon_m(x)$  by the inversion of Eq. (14.4). In the third step  $\varepsilon_m(x)$  is converted into the water content profile  $W(x)$  by standard transformations based on Eq. (14.1) or material-specific calibration functions. The first step as the key component for the reconstruction will be discussed in detail.

#### 14.4.1 The Telegraph Equations

The telegraph equations describe the variation of the voltage  $V(x,t)$  and the current  $I(x,t)$  in time along the transmission line. By applying Kirchhoff's voltage and current laws to the equivalent circuit in Fig. 14.5 the following is obtained:

$$\frac{\partial}{\partial x} V(x,t) = -R(x)I(x,t) - L(x)\frac{\partial}{\partial t} I(x,t) \quad (14.7)$$

$$\frac{\partial}{\partial x} I(x,t) = -G(x)V(x,t) - C(x)\frac{\partial}{\partial t} V(x,t). \quad (14.8)$$

In order to reconstruct the two parameters  $C(x)$  and  $G(x)$ , two independent measurements are needed. Consequently, the task is divided into two parts, one part dealing with an incident wave from one side and the other part dealing with an incident wave from the other side of the cable.

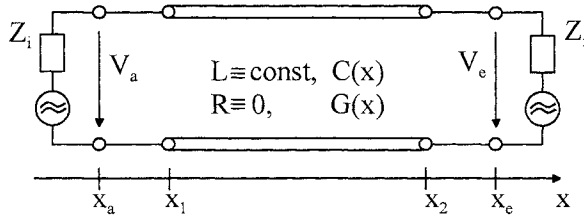


**Fig. 14.13.** The non-uniform flat band cable, situated between  $x_1$  and  $x_2$ , is connected to two lossless uniform coaxial cables with matched impedances  $Z_i$  at their endpoints and capacitances  $C_a$ ,  $C_e$  and inductances  $L_a$ ,  $L_e$ .

Figure 14.13 describes the set-up for receiving the reflection data from both sides of the unknown material. Therefore two separate measurements must be carried out with the external currents

$$F_{ex}^1 = \delta(x - x_a)f(t) \quad \text{and} \quad F_{ex}^2 = \delta(x - x_e)f(t). \quad (14.9)$$

The input data  $f(t)$ , which describes the incident pulse, can be easily extracted from the measurements  $V_a(t)$  of the coaxial cable between  $x_a$  and  $x_1$  with an open end at  $x_1$ .

The inverse method presented in the next section is based on an iterative search for the electrical parameters of the non-uniform flat band cable with the full-wave solution of both direct problems. During the search the solutions of the line need to be calculated many times. It is therefore important to use a technique that is computationally efficient, and which provides a simple mapping from the parameters to the direct solution, to guarantee a fast convergence.

Equations (14.7-8) can easily be transformed into a partial differential equation (PDE) of second order for  $V_i(x,t)$  representing the voltages of each separate experiment with regard to  $F_{ex}^i$ ,  $i=1,2$

$$\left[ LC \frac{\partial^2}{\partial t^2} + LG \frac{\partial}{\partial t} + \frac{\partial L / \partial x}{L} \frac{\partial}{\partial x} - \frac{\partial^2}{\partial x^2} \right] V_i(x,t) = 0, \quad i=1,2 \quad (14.10)$$

with the initial conditions

$$V_i(x,t)|_{t \leq 0} = 0, \quad \frac{\partial}{\partial t} V_i(x,t) \Big|_{t \leq 0} = 0, \quad x_a \leq x \leq x_e, \quad i=1,2. \quad (14.11)$$

The boundary conditions depend on the location of the external current  $F_{ex}^i(x,t)$ ,  $i=1,2$ . For the source at  $x = x_a$ , there is an absorbing boundary condition at  $x = x_e$

$$\left[ \frac{\partial}{\partial x} + \sqrt{L_e C_e} \frac{\partial}{\partial t} \right] V_1(x,t) \Big|_{x=x_e} = 0, \quad t \geq 0 \quad (14.12)$$

and an absorbing boundary condition for the reflected wave at  $x = x_a$  in connection with the external current:

$$\left[ \frac{\partial}{\partial x} - \sqrt{L_a C_a} \frac{\partial}{\partial t} \right] V_1(x,t) \Big|_{x=x_a} = L_a \frac{\partial}{\partial t} F_{ex}^1(x,t) \Big|_{x=x_a}, \quad t \geq 0. \quad (14.13)$$

For the other PDE for  $V_2(x,t)$  with external current  $F_{ex}^2(x,t)$  the boundary conditions are exchanged.

#### 14.4.2 The Optimization Approach

The aim of the investigation is the determination of the unknown distributions of  $C(x)$  and  $G(x)$  with measurements of input data  $f(t)$  and output data in the time domain. The output data  $\lambda_i(t)$ ,  $i=1,2$  ( $\lambda_1(t) = V_a(t)$ ,  $\lambda_2(t) = V_e(t)$ ) can be received from the two separate measurements with the external current  $F_{ex}^1$  and  $F_{ex}^2$ , respectively.

A cost function  $J(C,G)$  is defined which measures the difference in the  $L_2$ -norm between the solutions  $V_i(x_i,t)$ ,  $i = 1,2$  of the direct problems (Eqs. (14.10-13)) corresponding to the parameters  $C(x)$  and  $G(x)$  and the given measurements

$$J(C,G) = \sum_{i=1}^2 \int_0^T [V_i(x_i,t) - \lambda_i(t)]^2 dt \tag{14.14}$$

with  $T = 2\tau(x_1,x_2)$ , where  $\tau(x_1,x_2)$  is the travel time between  $x_1$  and  $x_2$ . The cost function refers to the error in the solutions  $V_1(x_1,t)$  and  $V_2(x_2,t)$ , respectively. The concept of the method is to find the parameter distributions  $C(x)$  and  $G(x)$  that minimize the cost function  $J$ . If the inverse problem has a solution the theoretical minimum of  $J$  is zero. One more important reason for choosing the  $L_2$ -norm is that this makes it possible to derive exact expressions for the gradient of  $J$ .

### 14.4.3 Exact Expression for the Gradient of the Cost Function

It is advisable to derive the gradient of  $J$  with respect to  $C$ ,  $J_C$ , by  $\lim_{\|\delta C(x)\| \rightarrow 0} (J(C+\delta C) - J(C)) =: (J_C, \delta C(x))$  where  $\delta C(x)$  denotes the differential of  $C(x)$  and  $(f,g)$  is the inner product defined by

$$(f(x), g(x)) = \int_{x_1}^{x_2} f(\xi)g(\xi)d\xi . \tag{14.15}$$

Thus, the gradient  $J_C(x)$  is the direction in which  $J$  increases most rapidly with respect to the norm of the change of the function  $C(x)$ .  $J_C(x)$  and  $J_G(x)$  are given by

$$J_C(C,G) = - \sum_{i=1}^2 \int_0^T \left( \frac{\partial}{\partial t} \Psi_i \right) \left( L \frac{\partial}{\partial t} V_i \right) dt \tag{14.16}$$

$$J_G(C,G) = \sum_{i=1}^2 \int_0^T \Psi_i \left( L \frac{\partial}{\partial t} V_i \right) dt \tag{14.17}$$

where the dual functions  $\Psi_1$  and  $\Psi_2$  satisfy the following PDEs:

$$\left[ LC \frac{\partial^2}{\partial t^2} - LG \frac{\partial}{\partial t} - \frac{\partial L}{\partial x} \frac{\partial}{\partial x} - \frac{\partial^2}{\partial x^2} \right] \Psi_i(x,t) = 2\delta(x - x_i)[V_i(x,t) - \lambda_i(t)], \quad i = 1,2 \tag{14.18}$$

with the initial conditions for  $t > T$  and boundary conditions similar to Eqs. (14.11-13).

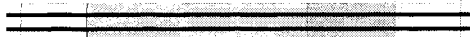
### 14.4.4 Reconstruction of the Parameters

Only reflection data is used to determine uniquely the parameters  $C(x)$  and  $G(x)$  [13]. The optimization is carried out with a conjugate gradient method using Fletcher-Reeves update formulas [14]. To determine the optimal step size  $\alpha$  for the search direction a parabolic approximation technique is used in each conjugate gradient step.

The initial capacitance  $C_0 = \tau^2(x_1, x_2)/(L(x_2-x_1)^2)$  can easily be determined by simple travel time measurements along the probe [15]. To ensure the invariability of this sensor travel time during the conjugate gradient algorithm one has to find a constant shift  $C_\alpha$  for every given  $\alpha$  during the optimization to fulfill

$$\sqrt{C_0}(x_2 - x_1) = \int_{x_1}^{x_2} \sqrt{C(x) + \alpha J_C(C, G) + C_\alpha} dx . \tag{14.19}$$

The result of the minimization of Eq. (14.14) is the spatial distribution of the total capacitance  $C$  and total conductance  $G$ .  $C(x)$  can easily be transformed into the dielectric properties  $\epsilon_m(x)$  of the surrounding material. Furthermore, the volumetric water content  $W(x)$  can be determined using standard transformations or a special calibration function for the material used. The total conductance  $G(x)$  describes the conductivity of the material between the copper wires, i.e., the system of polyethylene insulation and the surrounding material. The determination of the water content distribution of the surrounding material does not require knowledge of the conductivity distribution of the material, but it cannot be neglected during the reconstruction of  $C(x)$ .

C in pF/m	20	40	80	20	
G in S/m (lossy case)	0	0.004	0.008	0	
Left side					Right side
Section length	0.3 m	1.0 m	0.4 m	0.3 m	

**Fig. 14.14.** Inhomogeneous transmission line with four sections. Lossless case:  $C$  as indicated,  $G \equiv 0$ . Lossy case:  $C$  and  $G$  as indicated

### 14.4.5 Reconstruction Examples

The performance of the reconstruction algorithm will be demonstrated with an example. Consider the inhomogeneous transmission line shown in Fig. 14.14. The transmission line consists of four sections. Two different arrangements will be investigated. In the lossless case  $G$  is zero everywhere whereas in the lossy case  $G$  is non-zero in the two sections in the middle. The incident signal is shown in Fig. 14.15.

#### 14.4.5.1 Lossless Case

The TDR reflections from the left side and the right side are shown in Fig. 14.16. For each simulation the other side of the cable is left open, which results in a total reflection occurring at about 22 ns. In this simple example, the variation of the capacitance can roughly be estimated from the amplitude variations. High amplitude means low capacitance and vice versa.

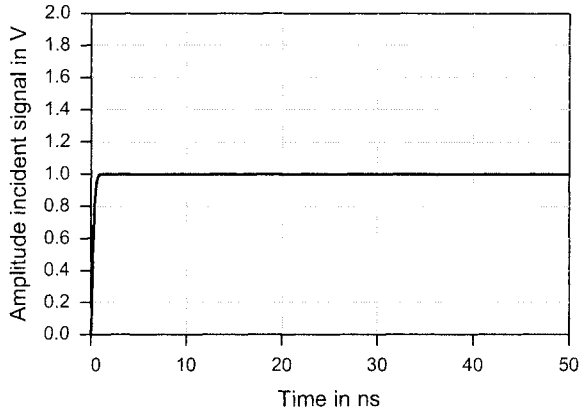


Fig. 14.15. Incident signal (step with a 10% to 90% rise time of about 460 ps)

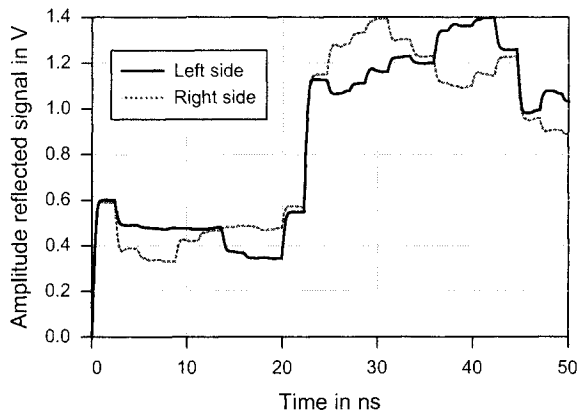


Fig. 14.16. TDR reflections from left and right side for the lossless case

Of course the reconstruction algorithm is more accurate, because it takes into account multiple reflections. In the lossless case only one parameter, namely,  $C(x)$  has to be reconstructed. Therefore it is sufficient to use only one-sided reflection data. The reconstruction shown in Fig. 14.17 is in close agreement with the true capacitance profile. Only at the sharp edges of the profile is some overshoot visible.

data. The reconstruction shown in Fig. 14.17 is in close agreement with the true capacitance profile. Only at the sharp edges of the profile is some overshoot visible.

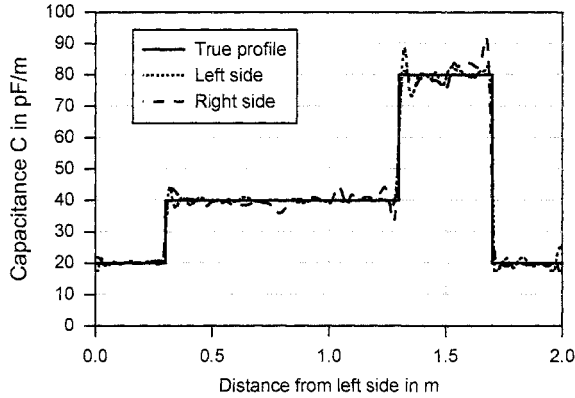


Fig. 14.17. Reconstruction of  $C(x)$  from one-sided data (left and right) in the lossless case

#### 14.4.5.2 Lossy Case

Figure 14.18 shows the TDR reflections for the lossy case. Losses reduce signal energy and decrease amplitude. The pronounced downward slope prevents prediction of the capacitance profile by simple visual inspection of the amplitude variation.

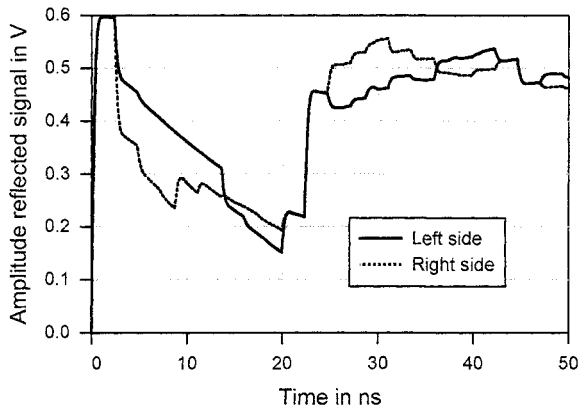


Fig. 14.18. TDR reflections from left and right side for the lossy case



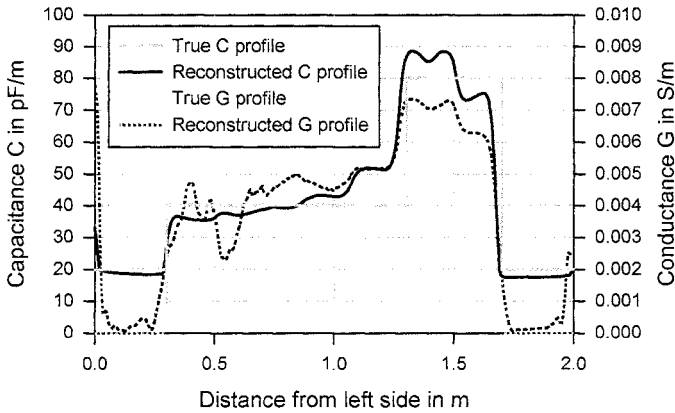


Fig. 14.19. Reconstruction of  $C(x)$  and  $G(x)$  from two-sided data in the lossy case

In the lossy case, our reconstruction algorithm requires reflection data from both sides of the cable to achieve reasonable accuracy. The results shown in Fig. 14.19 approximate the true profile  $C(x)$  and  $G(x)$  well.

## 14.5 A Novel TDR Measurement Principle

The overall costs of a soil moisture measurement system strongly depend on the cost of the TDR instrument. Commercially available TDR instruments are too expensive for widespread use in operational monitoring of soil moisture. Also they often lack the necessary robust design for long-term application under field conditions. To improve this situation a new TDR instrument “Observer” has been developed in collaboration with the ADD Automation company (Fig. 14.20).

### 14.5.1 The “Binary Sampler”, a Delta Modulator in Equivalent-Time Sampling

The Observer is a unique TDR, because it differs significantly from conventional instruments. Its sampler is based on the recently developed “Binary Sampler” [16]. The Binary Sampler is a differential pulse code or delta modulator [17]. A delta modulator is a codec (encoder/decoder), which encodes the error between the input signal and a prediction with 1-bit resolution, e.g., the signal is greater or less than the last prediction. It tries to minimize this error continuously by correcting the prediction. An integrator is used as first-order predictor. If the input at one sample instant is greater than the last prediction, the integrator will predict the input signal to be even larger at the next sample instant, and vice versa. The result of a delta modulator is a differential pulse code. It is transmitted to a receiver, e.g., a microcontroller, where it has to be digitally integrated to reconstruct the sampled

signal. The delta modulator itself has a local analog integrator as decoder, whose output is coupled back and used as a prediction for the input signal at the next sample instant. Therefore it is a control system which is different to the usual sampling bridge or gate circuits found in conventional samplers [18].

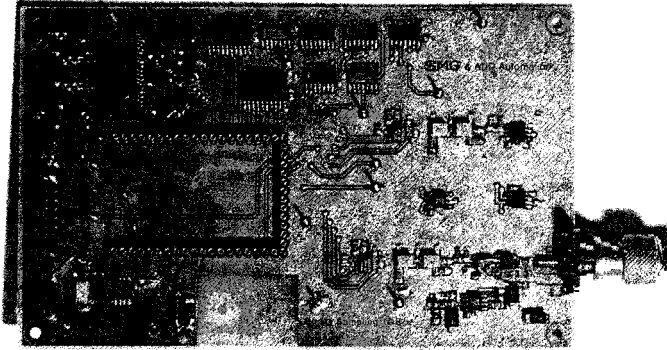


Fig. 14.20. Prototype of the new TDR instrument “Observer”

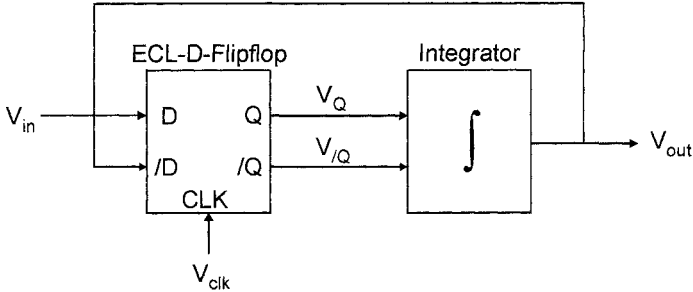


Fig. 14.21. Simplified block diagram of the Binary Sampler

The core of the Binary Sampler consists of two main functional blocks: an edge triggered D-flip-flop (D-FF) of a fast emitter coupled logic family (ECL), and an integrator, the output of which is coupled back to the input of the D-FF (Fig. 14.21). A D-FF is a simple storage element. At each rising edge of the D-FF clock signal the logic input state is shifted to the output and latched. A change at the input does not influence the output, unless a clock pulse is fired. The ECL family uses differential input and output stages. The differential input of the D-FF consists of the two signals D and /D (not D). A logic “1” or “0” is represented by a positive or negative voltage difference between D and /D, respectively. The high-frequency signal under investigation,  $V_{in}$ , is connected to D, whereas /D is connected to the output  $V_{out}$  of the integrator. The commonly available, cost-effective ECL D-FF acts in principle like a specialized strobed comparator [19]. It

compares  $V_{in}$  and  $V_{out}$  at each rising edge of a clock pulse, which is the sampling strobe. If

$$\Delta V_{in} = V_{in} - V_{out} \tag{14.20}$$

is positive or negative, the output voltage difference

$$\Delta V_Q = V_Q - V_{IQ} \tag{14.21}$$

will have a positive or negative constant value, respectively. It is important that even a very small input voltage difference leads to a full-scale output voltage swing. In the next stage of the control system the integrator integrates  $\Delta V_Q$ , which is a fixed positive or negative value between two consecutive clock pulse edges occurring at time  $t_{n-1}$  and  $t_n$ :

$$\begin{aligned} V_{out}(t_n) &= \frac{1}{t_c} \int_{t_{n-1}}^{t_n} \Delta V_Q(t) dt + V_{out}(t_{n-1}) \\ &= \frac{1}{t_c} \Delta V_Q(t_{n-1})(t_n - t_{n-1}) + V_{out}(t_{n-1}) = \frac{\pm |\Delta V_Q|}{t_c} \frac{1}{f_{CLK}} + V_{out}(t_{n-1}). \end{aligned} \tag{14.22}$$

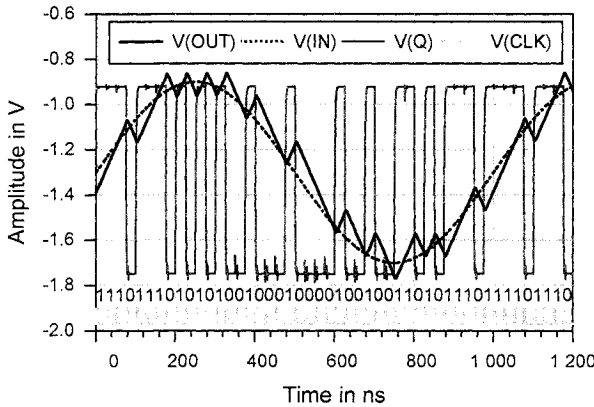


**Fig. 14.22.** Real-time sampling of a sinusoid by a delta modulator.  $V_{in}$ : input sine wave,  $f_{in}=1$  MHz,  $V_{clk}$ : sample clock,  $f_{clk} = 40$  MHz,  $V_{out}$ : feedback, piecewise linear approximation of  $V_{in}$ ,  $V_Q$ : Q-output of the D-FF. The sequence of the D-FF’s logic states is the pulse-coded signal (PSPICE simulation results)

Integration up to the next clock pulse time  $t_n$  adds a linearly rising or falling voltage ramp to the former voltage level  $V_{out}(t_{n-1})$ . The slope of the ramp is determined by the integrator’s time constant  $t_c$  and the constant voltage  $\Delta V_Q$ . The resulting voltage  $V_{out}$  is fed back to the /D input of the D-FF.

The working principle of this feedback can be best explained with an example (Fig. 14.22). Assume  $V_{in}$  to be greater than  $V_{out}$  at sampling time  $t_0$ :  $\Delta V_{in} = V_{in} - V_{out} > 0$ . Thus the output  $\Delta V_Q$  of the D-FF is set positive. This leads to a rising voltage ramp at the output of the integrator, which drives  $V_{out}$  toward  $V_{in}$ . The

output voltage does not change direction until at some sample strobe the feedback voltage  $V_{out}$  exceeds  $V_{in}$ , i.e.,  $\Delta V_Q = V_{in} - V_{out} < 0$ . Then the D-FF changes its output state and  $\Delta V_Q$  becomes negative, which leads to a falling feedback voltage correcting the error between input and feedback.

Thus the circuit always tries to minimize the input voltage difference as far as possible. In this respect it resembles the Sampling Voltage Tracker (SVT) of the American National Institute of Standards and Technology [20], but differs significantly from the SVT in the way the signal under test is coded. The SVT samples the same instant of the repetitive input signal over many periods and digitizes the analog feedback voltage with a high-resolution analog-to-digital converter, e.g., 18 bits per sample, giving the absolute voltage level. In contrast the Binary Sampler is a delta modulator and uses the logic state of the D-FF to code the signal, i.e., 1 bit per sample, giving just differential information, i.e., step up (logic 1) or step down (logic 0). The encoding of the signal leads to a bit stream, which has to be decoded by integration and filtered to reconstruct the signal. The differential pulse code leads to very effective data compression, since only one bit per sample is needed.

#### 14.5.2 Slope Overload, Amplitude Range, and Quantization Noise

The example of Fig. 14.22 shows a fairly rough approximation of the input sinusoid. To reduce the quantization error, the swing or step size of the integrator's output has to be reduced by an increase of its time constant. It is obvious that, without an increase of the sampling rate, the output signal cannot follow the steep edges of the sinusoid. When the slope of the input signal exceeds the maximum slope of the feedback signal a "slope overload" condition has been reached. Especially in TDR applications where a precise recording of steep rising edges of incident and reflected waves plays the essential role, slope overload is strictly to be avoided. To investigate the avoidance of slope overload, the input is assumed to be sinusoidal with amplitude  $A$  and frequency  $f_s$ :

$$V_{in}(t) = A \sin(2\pi f_s t). \quad (14.23)$$

Its maximum slew rate is given by the first derivative around its zero crossings. The condition of slope overload is generally avoided if the slew rate of the feedback (cf. Eq.(14.24)) is larger than the maximum slew rate of the input signal:

$$2\pi f_s A < \frac{1}{t_c} |\Delta V_Q|. \quad (14.24)$$

If the frequency of the input signal increases, the integrator's time constant has to be decreased to fulfill the condition for non-overload. Equation (14.24) can also be interpreted as a condition for the maximum allowable amplitude  $A_m$  of an input signal with bandwidth  $f_s$ . This determines the theoretical upper value of the sampler's amplitude range. The lower value is the smallest amplitude of a sinusoid which still disturbs the idling pattern of the sampler. The idling pattern is a regular

pattern of alternating rising and falling slopes, which occurs when the input signal is a constant. The amplitude of the idling pattern is

$$A_I = \frac{1}{2} \frac{|\Delta V_Q|}{t_c} \frac{1}{f_{clk}}. \quad (14.25)$$

The larger the input signal amplitude becomes with respect to Eq. (14.25), the better the tracking. According to Eqs. (14.24 and 14.25) the amplitude range covered by the delta modulator is:

$$R = \frac{A_m}{A_I} = \frac{f_{clk}}{\pi f_s} \quad (14.26)$$

This ratio is not really the dynamic range, since the minimum amplitude, which gives an acceptable decoded signal-to-noise ratio, is a subjective choice.

Each sampling process is accompanied by quantization noise which is due to quantized time and amplitude. The calculation of the quantization noise produced by delta modulators is not a trivial task. Only the simple formula for quantization noise derived by DeJaeger [21], is given here:

$$N_q^2 = K_q \frac{f_c \gamma}{f_{clk}} \quad (14.27)$$

$\gamma$  is the step size of integrator after one sampling period:

$$\gamma = \frac{|\Delta V_Q|}{t_c} \frac{1}{f_{clk}}. \quad (14.28)$$

$f_c$  is the bandwidth of the message band of the codec,  $K_q$  is an arbitrary constant. A detailed analytical derivation of an improved formula describing the quantization noise is given in [17] and a summary of this analysis in [22].

### 14.5.3 Equivalent-Time Sampling

Among other applications delta modulators have been used to encode speech in realtime [21, 23]. The Binary Sampler is a delta modulator running not in realtime but equivalent-time mode, like most conventional samplers used in oscilloscopes or TDRs. In equivalent-time sampling the complete sample of a repetitive, stationary signal is composed of interleaved samples taken over many signal periods. The Binary Sampler for example takes one sample per period and sweeps the sample instant slowly across the signal. Equivalent-time sampling enables the sampler to acquire signals up to the analog bandwidth of the sampling system regardless of the sample rate. Real-time sampling of signals with a bandwidth of a few gigahertz is a much higher technical and economical expense.

### 14.5.4 “Observer”, a Novel TDR Instrument Based on the Binary Sampler

The TDR prototype “Observer” is an application of this sampling technology. Figure 14.23 shows the block diagram. It mainly consists of a 1-bit sampler (delta modulator, Binary Sampler), two similar pulse generators, and two channels with different coding alternatives. In channel A the differential pulse code of the delta modulator is read. Every 8 bits, 1 byte is formed by means of a shift register. These bytes are buffered in a RAM, which is not shown in Fig.14. 23. The second channel B has just been added for test purposes. Here an analog-to-digital converter is used to digitize the feedback of the sampler, which yields a representation of absolute voltage levels rather than a differential pulse code.

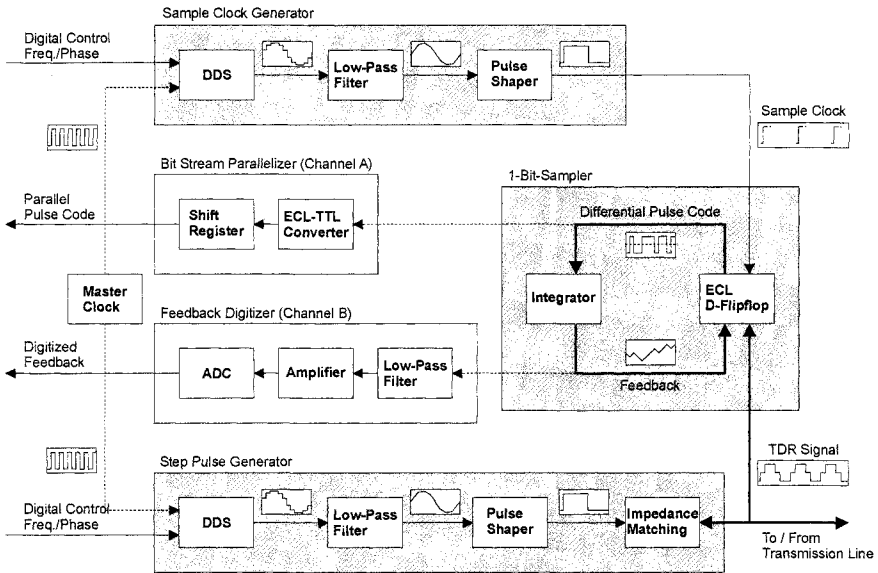


Fig. 14.23. Block diagram of the Observer

The two signal generators are driven by direct digital synthesis (DDS). The output frequency of the DDS can be programmed and controlled very precisely. The DDS produces a staircase approximation of a sinusoid, which has to be filtered to get the desired sine wave as pure as possible. The filtered sine wave enters a Schmitt trigger with hysteresis (“pulse shaper”) which puts out a square wave. Thus both signal generators produce square waves with programmable frequency. The sample clock generator generates the sampling strobes for the sampler. The step pulse generator is connected to the transmission line. The superposition of emitted and reflected pulses traveling along the transmission line reaches the input of the sampler.

To achieve equivalent-time sampling, the step generator and clock generator have to be detuned slightly. The clock frequency can be expressed in terms of the step generator frequency  $f_{step}$  and a small offset:

$$f_{clk} = f_{step} - f_{offset} \quad (14.29)$$

The offset frequency  $f_{offset}$  is chosen to be six to eight orders of magnitude less than  $f_{step}$  or  $f_{clk}$ . During each TDR signal period one sample is taken. Since the clock is a little bit slower than the step signal, the phase of the sample clock sweeps slowly across the TDR signal from sampling pulse to sampling pulse. After a time

$$t_s = f_{offset}^{-1} \quad (14.30)$$

step and clock pulse are in phase again, indicating that one complete period of the TDR signal has been sampled. The result is a sampled approximation of the TDR signal on a much longer time scale. The input signal period  $t_{step} = f_{step}^{-1}$  is dilated to the time scale  $t_s$ . The dilation factor is

$$s = \frac{t_s}{t_{step}} = \frac{f_{step}}{f_{offset}} \quad (14.31)$$

with  $10^6 \leq s \leq 10^8$ , typical for the application of soil moisture measurement. The sampling of one TDR period takes  $t_s$  seconds. During this time,  $n_{clk} = t_s f_{clk}$  sampling pulses occur. Thus one TDR signal of period  $t_{step}$  is sampled with  $n_{clk}$  points, yielding a theoretical temporal resolution of

$$\Delta t_r = \frac{t_{step}}{n_{clk}} = \frac{f_{offset}}{f_{step} f_{clk}} \approx \frac{f_{offset}}{f_{step}^2} \quad (14.32)$$

This theoretical resolution can easily be set down to  $\Delta t_r = 10^{-12}$  s. In reality the corresponding bandwidth cannot be reached, since it is limited by timing jitter, noise, and low-pass effects of the electronics.

### 14.5.5 Application and Comparison to Other Instruments

A wide range of different requirements for such a device exists even in the limited field of soil moisture measurement. In one application a moisture profile along a rod probe of a few centimeters may be needed, in another case the moisture distribution along a very extended system consisting of a flat band cable connected to a coaxial cable may have to be determined. To demonstrate the capabilities of the Observer, comparative measurements with two commercial TDRs have been performed. These instruments are the “1502B metallic cable tester” by Tektronix and the “TDR100” by Campbell Scientific. Both TDRs use conventional technology with sampling gates. The time base in these instruments is given by delay generators, which compare a linearly rising voltage ramp with variable slew rate to a given voltage threshold.

A 60 cm three-rod-probe has been vertically installed in a laboratory lysimeter. All three TDRs are connected to the probe via a multiplexer. The aim of the hydrological study was to demonstrate the possibility to track the temporal evolution of infiltration fronts propagating in the soil with TDRs. Figure 14.24 shows the TDR signal after 30 minutes of precipitation. The rising edge at 3 nanoseconds is the partial reflection at the probe's head. Approximately 10 nanoseconds later a strong reflection due to the probe's end is detected. In between the signal propagates along the rods buried in soil. The depression at the beginning of this part of the signal indicates the wet zone in the first centimeters of soil.

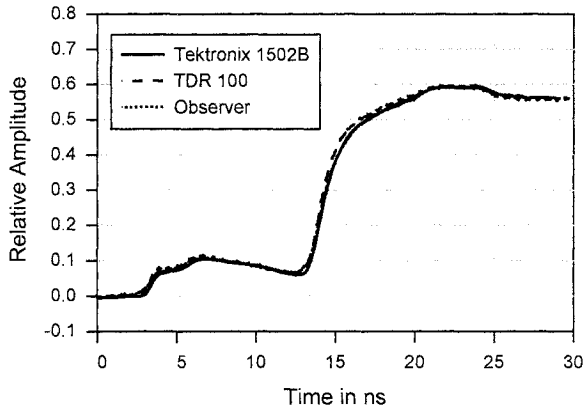


**Fig. 14.24.** First measurement results of the Observer in comparison to Tektronix cable tester 1502B and Campbell TDR100.

The good agreement between the simple prototype and the other TDR instruments is very promising. The main difficulty with the current design of the Observer is signal integrity issues, e.g., due to the noise generated in the crystal oscillator and in the power supply. Crosstalk disturbs the sampler feedback path and probably also increases the phase noise of the signal generators because of the high sensitivity of the zero cross detectors and the resulting uncertainty of the switching instant. It may be advisable to change the current design from DDS to PLL to avoid the sensitive pulse shaping. Another problem is a slow voltage drift of the TDR step generator, which looks like the charging and discharging of a capacitor, an effect not yet understood. Another concern is the phase stability between clock and step signal at low frequencies. Nevertheless we assume that with the Observer's concept an adequate performance for the desired applications can be achieved.



## 14.6 Experimental Results

### 14.6.1 Measuring of Soil Water on a Full-Scale Levee Model

The percolation of levees due to a hydraulic load from a flood or the infiltration of water during a precipitation event is currently being investigated [24]. For this investigation a full-scale levee model is available (cf. Fig. 14.25). The levee is built up homogeneously with uniform sand (grain size 0.2 to 2 mm) and it is based on a waterproof sealing of plastic, so that infiltrating water in the dike will flow to a drain at the landside slope. A basin has been included to provide the opportunity to simulate flood events.

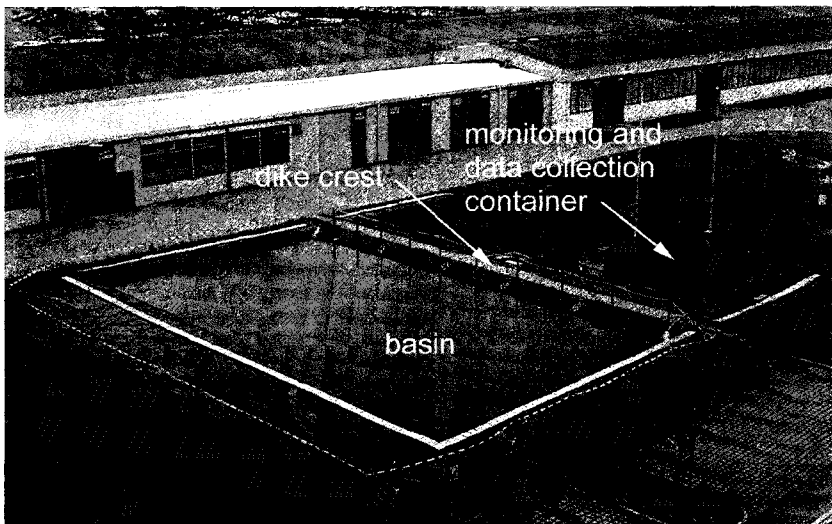


**Fig. 14.25.** Full-scale levee model at the Federal Waterways and Research Institute in Karlsruhe during a flood simulation test in December 2000 (steady state of seepage condition)

The aim of the project is the quantitative description of the influence of initial soil water distribution within the levee body on the progression of the percolation of water during a flood event. For this, the levee was equipped with 12 vertically installed flat band cables from 1 to 3 m in length, connected from both sides with coaxial cables to a multiplexer, and TDR device in a box on the crest of the levee. The data collection and controlling equipment (PC) of the multiplexer and the TDR device are placed in a measuring container at the toe of the landside slope (Fig. 14.26). With this system the data acquisition time for the whole cross-section is reduced to only 5 minutes. Subsequent processing of the time-dependent data into a spatial distribution, e.g., for the water content, requires several hours on a desktop PC. For the purpose of comparing the results there is the possibility of

measuring soil water profiles with conventional probes for tubes based on TDR. In addition to these TDR systems, pore water gauges are installed on the sealing at the base of the model in order to measure the hydraulic head inside the levee body.

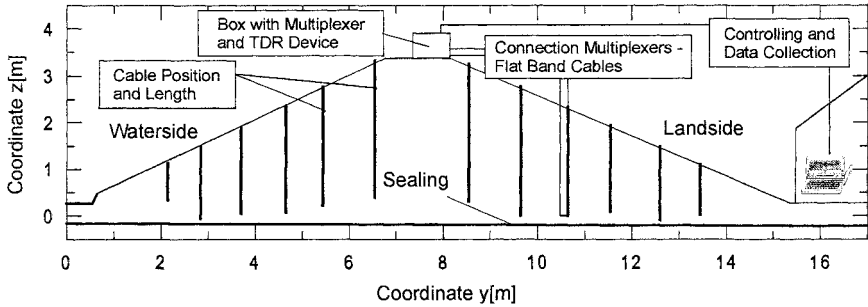


**Fig. 14.26.** Location of the flat band cables in the cross-section of the levee and schematic description of the measuring system

Figure 14.27 shows the results of measurements during a flood simulation test carried out with the levee model in December 2000. The top picture represents a result measured with a TDR probe for tubes and the picture below is measured with the flat band cables as transmission lines. The dotted lines represent the positions of the individual flat band cables together with the volumetric water content at these locations (see also the gray-scale bar in Fig. 14.27). For better visualization, the single measurements were interpolated over the observed area in the cross-section. The dark gray shows wet zones whereas the light gray represents the more dry zones. In addition, the levels of the hydraulic head are given in the figures representing the approximate position of the phreatic line inside the levee body. The independently measured water level in the basin is also marked.

At first glance one big advantage of the measuring system with the flat band cables can be recognized. While the flat band cables are able to measure the water content in the levee body under the water level of the basin, the tubes cannot be reached in order to make any manual measurements, which require about 1 hour. The measurement with the flat band cables needs only 5 minutes.

The discrete measurements with the probe for tubes determine a mean value for the soil water content over a length of about 20 centimeters. The results along the flat band cables are available in a resolution from 1 to 3 centimeters. In spite of these differences, the results of both measurements correspond well with the independently determined phreatic surface. The differences in the water content between both observation methods vary by about 3 vol %. The porosity of the levee material – this means the ratio of the pore volume to the whole volume – is about 37%, but the measured volumetric water content underneath the phreatic surface is lower. This means that there are air bubbles in the area percolated.

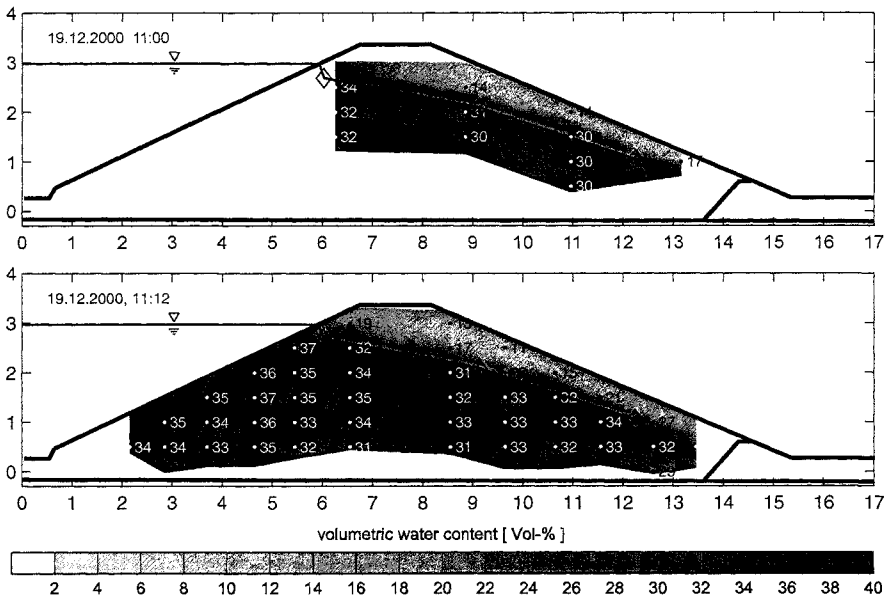


**Fig. 14.27.** Results of the volumetric water content distribution measured with a probe for tubes (top) and flat band cables as transmission lines (middle) with an independently measured phreatic surface inside the levee body and water level in the basin (steady state of seepage condition during a flood simulation test in December 2000)

Two results of a sprinkler irrigation test are shown in Fig. 14.28. In this experiment a precipitation event which occurs in Karlsruhe around every 100 years was simulated. The resulting rainfall of 140 mm was subdivided over three days each with 9 hours sprinkler irrigation from midnight to 9 a.m. In Fig. 14.28 (top) the initial soil moisture distribution can be seen before the first sprinkler irrigation and Fig. 14.28 (middle) shows the measurement result after the last one. It can be recognized that almost over the whole cross-section the volumetric water content has increased besides the area in the middle of the levee body. This non-uniform distribution of the water content with a declining value from the top down to the base of the levee was verified by independent measurements with tensiometers in the levee body. For the first time, the new TDR method using flat band cables as transmission lines has offered the possibility of a quantitative observation of transient hydraulic processes to a high resolution in both space and time.

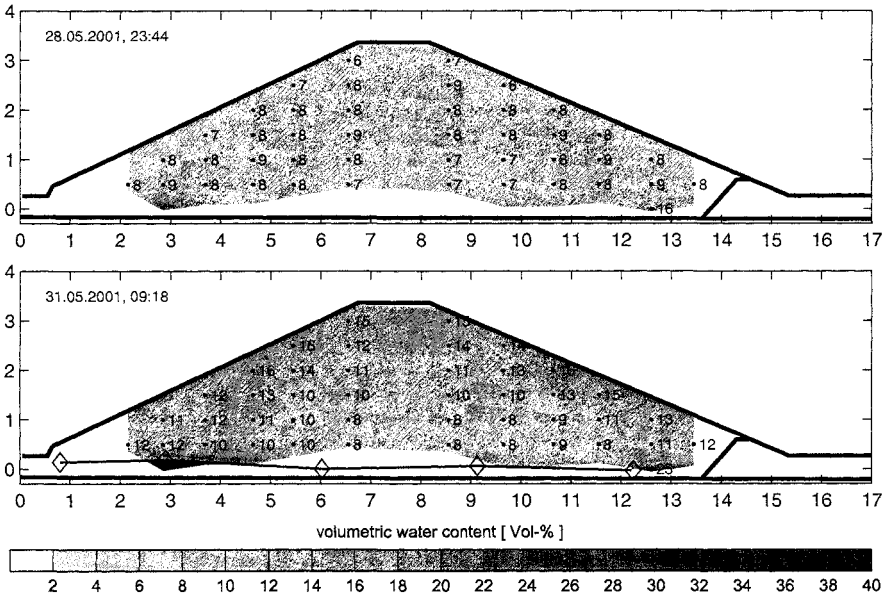


**Fig. 14.28.** Results of the volumetric water content distribution measured with flat band cables as transmission lines before a simulation of a precipitation event (top) and after the last sprinkler irrigation in May 2001 (middle)

## 14.6.2 Monitoring of Levees and Dams

At the Institute of Soil Mechanics and Rock Mechanics, University of Karlsruhe, large-scale infiltration tests were carried out on a cable sensor 30 m long, in order to test the suitability of the TDR measuring technique for assessing the water side sealing elements of levees or dams. For this investigation a sensor was inserted into a sand-filled pipe, which had been slit open at the top and perforated at the bottom. Water was sprinkled over the sensor at different positions and at varying widths. At the same time reflection measurements were carried out from both ends of the sensor, in order to improve the resolution accuracy. The aim is not to reconstruct the water content along the cable, as in the levee model at the BAW (cf. previous section), but to directly evaluate the measuring signals to localize any water content anomalies.

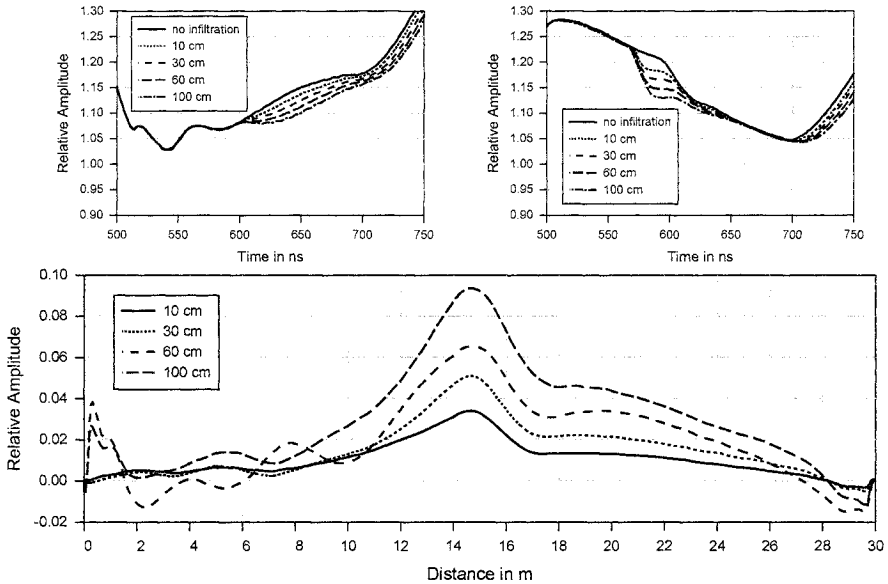


**Fig. 14.29.** Top: reflection measurements on both sides of a flat band cable 30 m long during an infiltration at  $x = 15$  m (i.e., in the middle of the cable) over different widths (10, 30, 60, and 100 cm). Bottom: transformation result of reflection measurements

At the top of Fig. 14.29 the reflection measurements are shown, which are carried out at both ends for infiltration over different widths (10, 30, 60, and 100 cm) at  $x = 15$  m. As can be seen from the curve in the left hand diagram (measurement from  $x = 0$  m), the area between  $x = 0$  m and  $x = 15$  m (corresponding to the time 500-600 ns) is hydraulically disturbed by prior infiltrations at  $x = 2$  m (510 ns),  $x = 5$  m (540 ns), and  $x = 10$  m (570 ns). The soil between  $x = 16$  m and  $x = 30$  m retained its original dry condition. As opposed to the measurement without infiltration, the changes in this section in the reflection signals originate only from the infiltrations at  $x = 15$  m. In the left hand diagram several of these changes start at 600 ns; however, in the right hand diagram they already start at 570 ns. This difference results from the slower velocity of the signal in a medium with a higher dielectric constant, i.e., with a higher soil water content. An exact localization of the soil water anomaly from a one-sided reflection measurement is thus hardly possible. However, if use is made of the information from both reflection measurements by

1. subtracting the initial signal from the time signals (without infiltration),
2. reflecting the corresponding right hand curve and superimposing it with the left one (by addition), and
3. transforming these resulting curves to the cable length,

a very good estimate of the position of the water content anomaly can be obtained (cf. Fig. 14.29, bottom). In comparison to a reconstruction of the water content, this estimate can be calculated quickly and without any great effort. Thus it is very well suited as an evaluation algorithm for a monitoring system. This monitoring system will first be used on the River Rhine in a zoned levee with mineral sealing on the water side and a drain at the toe of the land side slope [25].

## 14.7 Conclusion

Advanced measurement methods in TDR are presented that focus on three areas. First, a new transmission line technology has been developed which is based on insulated flat band cables and extends the maximum length of TDR transmission lines up to 10 m or more. The electrical parameters of the transmission lines have been investigated with numerical field calculations and incorporated into an electrical equivalent circuit. Second, a new algorithm for determining the water content distribution along transmission lines has been developed. It is based on TDR measurements from both sides of the transmission line and an optimization approach for determining the parameters of the telegraph equations. Third, a novel TDR instrument with binary sampling has been presented. It is a low-cost, high-performance alternative to conventional TDR devices.

The new reconstruction algorithm has been integrated into a soil moisture measurement system for investigating the water transport processes in a full-scale levee model. For this purpose flat band cables were installed in a levee and connected to a cable tester and data acquisition equipment. A simulation of a flood event was carried out. The spatial resolution had an accuracy of about 3 cm and the volumetric water content profiles along the cables were determined with an average deviation of  $\pm 2\%$  compared to independent measurements. Due to the data acquisition time for the TDR data of about 5 minutes for the complete cross-section of the levee, fast-running water transport processes could be monitored for the first time at this spatial resolution. Future improvements of the measurement system will include optimized processing of the TDR data and better soil specific calibration.

## References

1. Topp GC (2001) Electromagnetic wave measurements of soil water content: a state-of-the-art. In: Kupfer K, Hübner C (eds) Proceedings of the fourth international conference on electromagnetic wave interaction with water and moist substances, Weimar, Germany, May 13-16, pp 327-335
2. Topp GC, Davis JL, Annan AP (1980) Electromagnetic determination of soil water content: measurement in coaxial transmission lines. *Water Resour Res* 16:574-582
3. Birchak JR, Gardner CG, Hipp JE, Vicor JM (1974) High dielectric constant microwave probe for sensing soil moisture. *Proc IEEE* 62:93-98

4. Dobson MC, Ulaby FT, Hallikainen MT, El-Rayes MA (1985) Microwave dielectric behaviour of wet soil, II Dielectric mixing models. *IEEE Trans. Geosci, Remote Sensing* 23:35-46
5. Heimovaara TJ, Bouten W, Verstraten JM (1994) Frequency domain analysis of time domain reflectometry waveforms: 2. A four-component complex dielectric mixing model for soils. *Water Resour Res* 30:201-209
6. Heimovaara TJ (1994) Frequency domain analysis of time domain reflectometry waveforms: 1. Measurement of the complex permittivity of soils. *Water Resour Res* 30:189-199
7. Dalton FN, van Genuchten MTh (1986) The time domain reflectometry method for measuring soil water content and salinity. *Geoderma* 38:237-250
8. Huebner C, Brandelik A (2000) Distinguished problems in soil and snow aquametry. In: Baltes H, Goepel W, Hesse J (eds) *Sensors update*, vol 7, Wiley-VCH, Weinheim, pp 317-340
9. Huebner C, Brandelik A (2000) Near subsurface moisture sensing. In: Nguyen C (ed) *Subsurface sensing technologies and applications*, Proc SPIE 4129:88-96
10. Nyfors E, Vainikainen P (1989) *Industrial microwave sensors*. Artech House, Norwood, MA
11. Hook WR, Livingston NJ, Sun ZJ, Hook PB (1992) Remote diode shorting improves measurement of soil water by time domain reflectometry. *Soil Sci Soc Am J* 56:1384-1391
12. Schlaeger S (2002) Inversion von TDR-Messungen zur Rekonstruktion räumlich verteilter bodenphysikalischer Parameter. PhD thesis, University of Karlsruhe, Institute of Rock Mechanics and Soil Mechanics
13. He S, Romanov VG., Stroem S (1994) Analysis of the Green function approach to one-dimensional inverse problems. Part II: Simultaneous reconstruction of two parameters. *J Math Phys* 35:2315-2335
14. Fletcher R, Reeves CM (1964) Function minimization by conjugate gradients. *Comput J* 7:163-168
15. Heimovaara TJ, Bouten W (1990) A computer-controlled 36-channel time domain reflectometry system for monitoring soil water content. *Water Resour Res* 26:2311-2316
16. Monett MR (2004) <http://www3.sympatico.ca/add.automation/sampler/intro.htm> Feb 12
17. Steele R (1975) *Delta modulation systems*. Pentech Press, London
18. Mulvey J (1970) *Sampling oscilloscope circuits*. Tektronix, Beaverton, OR
19. Laug OB, Souders TM, Flach DR (1992) A custom integrated circuit comparator for high-performance sampling applications. *IEEE Trans Instrum Meas* 41:850-855
20. Souders TM, Hetrick PS (1988) Accurate RF voltage measurements using a sampling voltage tracker. *IEEE Trans Instrum Meas* 38:451-456
21. DeJaeger F (1952) Delta modulation – a new method of p.c.m. transmission using the 1 unit code. *Philips Res Rep* 8:442-446
22. Steele R (1980) SNR formula for linear delta modulation with band-limited flat and RC-shaped Gaussian signals. *IEEE Trans Commun* 28:1977-1984
23. Pohlmann KC (1995) *Principles of digital audio*. McGraw-Hill, New York
24. Scheuermann A, Schlaeger S, Hübner C, Brandelik A, Brauns J (2001) Monitoring of spatial soil water distribution on a full-scale dike model. In: Kupfer K, Hübner C (eds) *Proceedings of the fourth international conference on electromagnetic wave interaction with water and moist substances*, Weimar, Germany, May 13-16, pp 343-350
25. Scheuermann A, Brauns J (2002) Die Durchfeuchtung von Deichen – Modellversuche und Analyse. In: DGGT 12, Donau-Europäische-Konferenz, Proceedings, Passau, 197-200